THE JOURNAL OF PHYSICAL CHEMISTRY C
A JOURNAL OF THE AMERICAN CHEMICAL SOCIETY

Orthorhombic Symmetry and Anisotropic Properties of Rutile TiO_2

Nevill Gonzalez Szwacki,* Piotr Fabrykiewicz, Izabela Sosnowska, François Fauth, Emmanuelle Suard, and Radosław Przeniosło

Cite This: *J. Phys. Chem. C* 2023, 127, 19240−19249

Read Online

ACCESS | Metrics & More | Article Recommendations | Supporting Information

ABSTRACT: The symmetry of the material is an important factor determining its properties. In this work, we demonstrate both experimentally and by numerical simulations that the actual symmetry of the rutile phase of TiO_2 is orthorhombic, described with space group *Pnnm*, in contrast to what it is commonly believed that rutile TiO_2 has a tetragonal symmetry, described with space group $P4_2/mnm$. We present very precise first-principles calculations for the determination of the structural properties of rutile TiO_2 and highlight the relevance of using the revised regularized SCAN meta-GGA density functional for the interpretation and analysis of neutron and synchrotron radiation diffraction measurements. The lowering of the symmetry has a small but not negligible influence on the elastic, vibrational, and optical properties of rutile TiO_2.

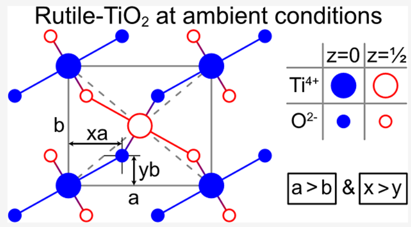

INTRODUCTION

Titanium dioxide can exist in different polymorphic forms: as tetragonal rutile, as anatase, or as rhombic brucite. However, rutile is the most stable polymorphic form of TiO_2.[1−3] In its pure form, rutile TiO_2 is colorless with a bluish tint, but depending on the impurities, it can be reddish-brown, sometimes yellowish, bluish, or violet. The characteristic feature that distinguishes rutile from other phases of TiO_2 is the large birefringence.[4] The refractive indices of rutile TiO_2 range from about 2.5−3.0 in the visible range of wavelengths.[5,6] TiO_2 is also a very chemically resistant compound.[7] Rutile TiO_2 has applications as a white pigment and a photocatalyst,[8,9] and it has interesting electronic and optical properties (see, e.g., ref 10). The photocatalytic splitting of H_2O by TiO_2 has become a paradigm for photocatalysis since its seminal discovery by Fujishima and Honda in 1972.[8] More recently, rutile TiO_2 films are also attracting attention as high-k dielectric materials for dynamic random access memory (DRAM).[11] These important applications of TiO_2 have stimulated a great deal of experimental and theoretical work on its properties.[7] A common feature of all of the previous studies related to rutile TiO_2 is that they assumed the tetragonal $P4_2/mnm$ symmetry of its crystal structure.[3,7,12] In this paper, we present a combined experimental and theoretical study that suggests that the symmetry of the crystal structure of rutile-type TiO_2 is orthorhombic, with a $CaCl_2$-type structure.[1] The assumed lower symmetry has implications for all of the properties of this material.

In order to better understand the structure and properties of rutile nanomaterials,[13] it is crucial to understand the structure of the bulk rutile. TiO_2 nanostructures can be synthesized directly from rutile minerals and industrial-grade rutiles (see, e.g., ref 14). Nanostructured rutile TiO_2 can be used for selective photocatalytic oxidation of aromatic alcohols to aldehydes in water (see, e.g., ref 15). Recent studies of the microfaceting process try to elucidate the nature of the surface reconstructions on rutile TiO_2 surfaces (see, e.g., ref 16). All of these processes, i.e., growth of rutile TiO_2 nanowires, specific chemical activity with molecules, and surface reconstruction are most probably related to the symmetry of the rutile crystal structure. An orthorhombic symmetry could explain an anisotropic behavior, e.g., along [110] and $[1\bar{1}0]$ directions compared with the tetragonal symmetry.

The high refractive indices at the visible wavelengths mentioned above are due to the high electronic polarizability of rutile TiO_2. On the other hand, rutile TiO_2 has high dielectric permittivities of 86 along *a*-axis and 170 along *c*-axis.[17] The high permittivity for the *c*-axis is due to the relative displacements between positive and negative ions described by the soft A_{2u} phonon mode. The ferroelectric A_{2u} phonon mode becomes softer with decreasing temperature; however, the crystal does not undergo a transition to the ferroelectric state even at temperatures reaching 0 K.[18] The experimentally observed direct band gap of rutile TiO_2 is 3.03 eV.[19] The band gap and other electronic and structural properties of rutile TiO_2 are not sufficiently well described within density functional theory (DFT) with local density approximation (LDA) and generalized gradient approximation (GGA).[20,21] The DFT approaches based on LDA and GGA predict for instance that anatase is more stable than rutile.[22] Some improvement can be achieved when using more sophisticated

Received: July 7, 2023
Revised: August 30, 2023
Published: September 15, 2023

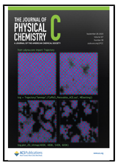

https://doi.org/10.1021/acs.jpcc.3c04573
J. Phys. Chem. C 2023, 127, 19240−19249

DFT approaches including hybrid functionals, DFT plus the Hubbard U correction (DFT + U), and dispersion-corrected DFT methods.[22,23] The self-interaction error (SIE) has long been identified as one of the limitations of practical density functional approximations.[24] In addition to SIE, yet another source of errors may be the assumed symmetry of rutile TiO_2 in the theoretical calculations and in the analysis of the experimental results. To explore the properties of TiO_2, we decided to go beyond the standard DFT calculations that can be found in the literature[18,20,25,26] for rutile-type TiO_2. As we argue in this work, the change of symmetry from tetragonal to orthorhombic can provide a more accurate description of the properties of rutile TiO_2. This paper is a continuation of earlier studies of a few other materials also ascribed to the rutile-type structure: β-MnO_2, MnF_2,[27] and β-PbO_2.[28]

METHODS

Theoretical Methods. The pseudopotential plane-wave-based DFT calculations have been done using the Quantum-ESPRESSO package.[29] The numerical methodology of those calculations is given in the Supporting Information. Our all-electron DFT calculations were performed using the highly accurate full potential linearized augmented plane-wave (FP-LAPW) method as implemented in the Elk code.[30] For the exchange−correlation (XC) potential, we have used the Perdew−Zunger (PZ),[31] the Perdew−Burke−Ernzerhoft (PBE),[32] and the revised PBE for solid (PBEsol)[33] functionals and also the r++SCAN functional, which is a more recent variant of the strongly constrained and appropriately normed (SCAN) meta-generalized gradient approximation (meta-GGA) exchange−correlation functional.[34] The r++SCAN functional, which is available through an interface to the Libxc library,[35] largely improves SCAN's numerical performance while keeping its high accuracy for lattice constant prediction for solids.[34] Basis functions are expanded in combinations of spherical harmonic functions inside non-overlapping spheres at the atomic sites (muffin-tin spheres) and in plane waves in the interstitial regions. The muffin-tin radii for oxygen (O) and titanium are taken to be 1.56 and 2.08 au, respectively. The interstitial plane-wave vector cutoff K_{max} is chosen such that $R_{mt}K_{max}$ equals 9 for all of the calculations (R_{mt} is the smallest of all atomic sphere radii). The convergence parameter $R_{mt}K_{max}$ controls the size of the basis. The valence wave functions inside the spheres are expanded up to $l_{max} = 10$, while the charge density was Fourier expanded up to $G_{max} = 18$. We found the optical spectra to be sufficiently well converged with a $11 \times 11 \times 17$ **k**-point grid (324 and 189 **k**-points for the $Pnnm$ and $P4_2/mnm$ crystal symmetries, respectively) in the irreducible Brillouin zone (BZ), and self-consistency was achieved by an iterative process with energy convergence up to 2.72×10^{-5} eV. The highest-accuracy `vhighq` option in Elk is used for accurate stress tensor calculations during structural optimization of both atomic positions and lattice vectors. The phonon frequencies are calculated for the Γ-point of BZ by using the finite-displacement method (supercell method).

Materials and Experimental Methods. Two commercial powder samples of rutile TiO_2 provided by Alfa Aesar (referred to as S1) and Aldrich (referred to as S2) were used for synchrotron X-ray powder diffraction (SXRPD) studies. Powder patterns were collected at the BL04-MSPD beamline[36,37] of ALBA synchrotron in the MYTHEN position sensitive setup.[38] The X-ray wavelength 0.44275(4) Å was calibrated using Si NIST standard reference. The measured angular range $4° < 2\theta < 50°$ corresponds to the scattering vector range 0.16 Å$^{-1} < Q < 1.90$ Å^{-1}. We use the convention of the scattering vector Q calculated as $Q = (2/\lambda)\sin\theta = 1/d$, where 2θ is the scattering angle and d is the inteplanar distance. The powder TiO_2 samples S1 and S2 were sealed in borosilicate capillaries of 0.5 mm diameter for SXRPD measurements at room temperature (RT). The instrumental contribution to peakwidths was determined by measuring a $Na_2Ca_3Al_2F_{14}$ reference standard.[39] Sample S1 contains only the rutile phase, and sample S2 contains 5.5(2)% mass of anatase. Anatase fraction in sample S2 was refined, but the structural parameters of anatase were not analyzed in the present study.

The powder TiO_2 sample S1 was also characterized by neutron powder diffraction (NPD) at 10, 150, and 300 K using the high angular resolution diffractometer D2B at the Institut Laue Langevin in Grenoble. The powder sample S1 was placed in 8.5 mm diameter thin-walled vanadium container. The measurements were done with open collimation in the 2θ range $10° < 2\theta < 160°$; however, we have analyzed the data for $10° < 2\theta < 122°$ because of the less good resolution at high 2θ angles. The analyzed 2θ range corresponds to 0.11 Å$^{-1} < Q < 1.10$ Å^{-1}.

The NPD diffraction pattern of rutile TiO_2 sample S1 at RT was used for wavelength calibration. By using the lattice constants determined with SXRPD on the same sample at RT the neutron wavelength of 1.5947(1) Å was determined.

The synchrotron radiation (SR) and neutron powder diffraction data were analyzed by using the aniostropic Bragg peak broadening model. The Bragg peaks were fitted with a pseudo-Voigt profile. The obtained integral breadths, β and full widths at half-maximum, FWHM were determined by using the program WinPLOTR.[40] We have also done full-pattern Rietveld refinements[41,42] using the programs Jana2006[43] and FullProf.[44]

RESULTS AND DISCUSSION

Pseudopotential Plane-Wave-Based Method. To study the possible lowering in the symmetry of rutile TiO_2, which is suggested by our experiment, it is assumed that the crystal structure of the rutile TiO_2 phase is described by the space group $Pnnm$ with Ti atoms occupying 2a sites (0, 0, 0) and with the O atoms occupying 4g sites $(x, y, 0)$. A good measure of the degree of distortion is given by the r_{ab} parameter, which is the relative difference of lattice parameters (in orthorhombic setting)

$$r_{ab} = 2\frac{a - b}{a + b} \tag{1}$$

and the r_{xy} parameter, which is the relative difference of the refinable position coordinates of oxygen $(x, y, 0)$

$$r_{xy} = 2\frac{x - y}{x + y} \tag{2}$$

It was reported in the literature[23] that the combined use of van der Waals interactions and the Hubbard U term for the Ti 3d orbital in the DFT calculations correctly reproduces the relative stability of rutile, brookite, and anatase. There are also recent reports in the literature[45] that employ DFT + U to study, among others, the electronic properties of TiO_2 polymorphs. Therefore, besides standard exchange−correla-

Table 1. Comparison of Structural Parameters Obtained within the Pseudopotential Plane-Wave Method for the *Pnnm* and $P4_2/mnm$ Models of Rutile TiO_2[a]

	LDA (PW)		GGA (PBEsol)		vdW-DF (rVV10)	
	Pnnm	$P4_2/mnm$	*Pnnm*	$P4_2/mnm$	*Pnnm*	$P4_2/mnm$
a	4.54385	4.54386	4.58281	4.58263	4.64331	4.64040
b	4.54373	4.54386	4.58251	4.58263	4.63832	4.64040
c	2.91738	2.91657	2.93737	2.93737	2.98160	2.98150
ΔE_{tot}	0.034		0.002		0.004	
r_{ab}	0.00003	0	0.00006	0	0.00107	0
x	0.30396	0.30394	0.30439	0.30433	0.30469	0.30426
y	0.30393	0.30394	0.30433	0.30433	0.30388	0.30426
r_{xy}	0.00010	0	0.00021	0	0.00266	0

[a] The lattice constants a, b, c are in angstroms and the total energy difference (ΔE_{tot}) is in meV per unit cell (6 atoms). The positive value of ΔE_{tot} indicates that *Pnnm*-TiO_2 is lower in energy. x and y are the fractional coordinates of oxygen ions. The experimental values for TiO_2 at 10 K are a = 4.5885(3) Å, b = 4.5849(3) Å, c = 2.9533(1) Å, x = 0.3075(10), and y = 0.3015(10) (see Table 5).

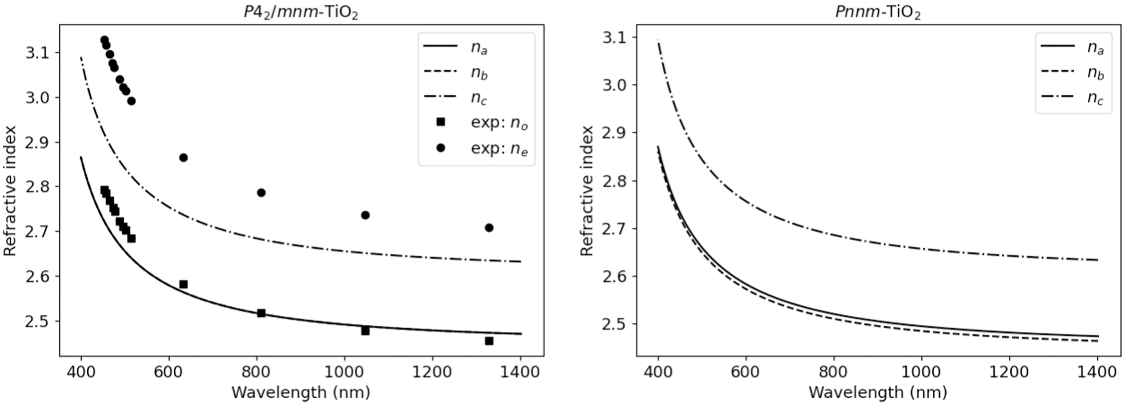

Figure 1. Refractive indices for tetragonal (left) and orthorhombic (right) rutile TiO_2 were obtained using the rVV10 functional and plotted as a function of the wavelength. At the left panel, we have also added experimental results for the ordinary (n_o) and extraordinary (n_e) refractive indices taken from ref 6 (adapted with permission from ref 6 Copyright 1997, AIP Publishing). At the right panel, the consequences of the lowering of symmetry are shown: the refractive index in the *ab*-plane is split into two values, n_a and n_b, along the *a*- and *b*-lattice directions, respectively.

Table 2. Calculated Elastic Constants C_{ij} (GPa), Bulk Modulus B (GPa), Young's Modulus E (GPa), Shear Modulus G (GPa), and Poisson's Ratio v for Rutile *Pnnm*-TiO_2 Together with Experimental Results at Room Temperature (RT) and 4 K

C_{11}	C_{22}	C_{33}	C_{12}	C_{13}	C_{23}	C_{44}	C_{55}	C_{66}	B	E	G	v	note
278.4	278.0	495.1	197.3	165.3	165.9	120.7	119.7	231.5	229.5	286.9	111.4	0.288	PBEsol
265.8	262.9	454.4	187.3	151.7	148.8	116.0	115.8	217.3	214.2	272.5	106.1	0.284	rVV10
							experiment						
268		484	175		147	123.8		190.2	212		113	0.274[b]	ref 46 (RT)
271.4		484.0	178.0	149.6		124.4		194.8	215.5	287.4[a]	124.4	0.258[b]	ref 47 (RT)
288.6			197.0					227.2					ref 47 (4 K)
									230				ref 48 (RT)

[a] From eq 5 in ref 47. [b] $v = (3B - 2G)/(6B + 2G)$.

tion functionals (PW and PBEsol), we used a vdW-DF functional (rVV10) in our pseudopotential calculations. We have also tested the DFT + U approach with U = 3, 6, and 9 eV. To our surprise, the obtained parameters r_{ab} and r_{xy} were very close to those for U = 0.

In Table 1, the computed equilibrium lattice parameters are listed for three exchange−correlation functionals. The deviation from the experimental lattice constants is about 1% at most. Our pseudopotential calculations predict modest but not negligible structural distortions for rutile-type TiO_2. Moreover, there is no substantial difference between the PW and PBEsol functionals and the rVV10 functional in the description of the structural properties of rutile TiO_2. The parameter r_{xy} is underestimated but is the closest to the measured values for the vdW-DF method. The GGA functional corrects the LDA disagreement with the experiment concerning the r_{xy} parameter, but the GGA result is only marginally better that the LDA result. Both LDA and GGA underestimate the unit cell volume, whereas vdW-DF overestimates it. The results for $P4_2/mnm$-TiO_2 are in excellent agreement with previous density functional calculations.[18,20,26]

An important and often used property of TiO_2 is a very high refractive index.[6] The experimentally obtained ordinary and extraordinary refractive indices plotted as a function of the wavelength are shown in the bottom panel of Figure 1. The computed refractive indices for tetragonal and orthorhombic TiO_2 plotted as a function of wavelength are also shown in Figure 1. The refractive index in the *ab*-plane has for each

Table 3. Comparison of the Structural Parameters Obtained within the Highly Accurate All-Electron FP-LAPW Method for *Pnnm* and $P4_2/mnm$ Models of Rutile TiO_2[a]

	PZ		PBE		PBEsol		r++SCAN		
	Pnnm	$P4_2/mnm$	*Pnnm*	$P4_2/mnm$	*Pnnm*	$P4_2/mnm$	*Pnnm*	$P4_2/mnm$	experiment
a	4.5462	4.5457	4.6386	4.6381	4.5838	4.5849	4.5916	4.5772	4.5886(3)
b	4.5443	4.5457	4.6362	4.6381	4.5829	4.5849	4.5653	4.5772	4.5849(3)
c	2.9207	2.9216	2.9686	2.9690	2.9424	2.9426	2.9534	2.9553	2.9533(1)
ΔE_{tot}	7.2		8.0		7.8		9.1		
r_{ab}	0.0004	0	0.0005	0	0.0002	0	0.0057	0	0.0008(1)
x	0.3042	0.3040	0.3054	0.3053	0.3046	0.3045	0.3054	0.3032	0.3075(9)
y	0.3040	0.3040	0.3053	0.3053	0.3045	0.3045	0.3009	0.3032	0.3015(10)
r_{xy}	0.0007	0	0.0005	0	0.0005	0	0.0148	0	0.020(1)

[a] The lattice constants a, b, and c are in angstroms, and the total energy difference (ΔE_{tot}) is in meV per unit cell (6 atoms). The positive value of ΔE_{tot} indicates that *Pnnm*-TiO_2 is lower in energy. x and y are the fractional coordinates of oxygen ions. The experimental values are taken from Table 5.

Table 4. Calculated Γ-Point Phonon Frequencies (in cm^{-1}) of Bulk *Pnnm*-TiO_2 Compared to Available Experimental Data, Which Assumes That TiO_2 Has $P4_2/mnm$ Symmetry[a]

mode		theory				experiment	
Pnnm	$P4_2/mnm$	PBE	PBEsol	PZ	r++SCAN	neutrons	IR and Raman
A_u (S)	B_{1u} (S)	1.9	53.0	97.3	94.4	113	
A_g (R)	B_{1g} (R)	156.4	145.2	125.7	115.4	142	143 (143)
B_{3u} (I)	E_u (I)	1.3	84.3	131.5	156.2	189	183
B_{2u} (I)		1.6	86.2	132.2	159.3		
B_{1u} (I)	A_{2u} (I)	i37.3	68.2	140.7	178.8	173 (142)	167 (144)
B_{2u} (I)	E_u (I)	353.9	366.4	381.3	394.3	not found	388
B_{3u} (I)		354.1	366.6	381.6	398.3		
A_u (S)	B_{1u} (S)	358.3	375.9	392.7	415.9	406	
B_{1g} (R)	A_{2g} (S)	420.7	418.6	422.0	432.2	not found	
B_{2g} (R)	E_g (R)	429.9	448.5	464.6	460.7	445	447 (455)
B_{3g} (R)		430.3	448.9	464.7	460.7		
B_{2u} (I)	E_u (I)	467.7	476.1	485.2	493.2	494	500
B_{3u} (I)		468.3	476.4	485.5	494.0		
A_g (R)	A_{1g} (R)	565.5	589.8	611.0	610.2	610	612 (611)
B_{1g} (R)	B_{2g} (R)	769.9	796.0	818.1	827.0	825	827

[a] The inelastic neutron scattering data are taken from ref 12, and the Raman and infrared (IR) data are taken from refs 54−56, respectively. The values given in parentheses correspond to frequencies measured at low temperature (4 K). The Raman-active, IR-active, and inactive modes are labeled by R, I, and S, respectively.

wavelength only one value in the case of tetragonal TiO_2 (see the left panel of Figure 1), whereas it is split into two values, n_a and n_b, along the a- and b-lattice directions, respectively, for the case of orthorhombic TiO_2 (see the right panel of Figure 1).

Table 2 represents the comparison of calculated elastic constants (C_{ij}), bulk modulus (B), Young's modulus (E), shear modulus (G), and Poisson's ratio (ν) for rutile *Pnnm*-TiO_2 with experimental results.[46−48] The theoretical values for B, E, G, and ν are calculated using the Voigt−Reuss−Hill approximation.[49] We have verified that our calculated elastic constants C_{ij} satisfy the necessary and sufficient elastic stability criteria (Born conditions) for an orthorhombic system.[50] Although the anisotropy (e.g., $C_{11} \neq C_{22}$) at the PBEsol level is tiny (C_{11} = 278.4 GPa and C_{22} = 278.0 GPa), assuming lower symmetry one gets a more consistent agreement between theoretical and experimental values than previously reported[51] for rutile $P4_2/mnm$-TiO_2. Furthermore, according to our results at the rVV10 level, the anisotropy of the elastic constants is not negligible: C_{11} = 265.8 and C_{22} = 262.9 GPa. We also get a very good result for the bulk modulus, B = 214.2 GPa, which is very close to the experimental value of B = 215.5 GPa reported in ref 47.

Highly Accurate All-Electron FP-LAPW-Based Method. Motivated by the recent success of the SCAN family of exchange−correlation functionals in describing the properties of TiO_2,[24,52,53] we have employed the r++SCAN to study the structural properties of TiO_2. In Table 3, the equilibrium lattice parameters are listed for r++SCAN and three other exchange−correlation functionals. All of the results for the lattice constants are in reasonable agreement with the experiment. The parameter r_{xy} is very close to the measured value for the r++SCAN functional. We notice that the PZ functional corrects the PBE and PBEsol disagreement with the experiment concerning the r_{xy} parameter, but the PZ result is only marginally better than the PBE and PBEsol results. The PZ, PBE, and PBEsol functionals underestimate the r_{ab} parameter, whereas r++SCAN overestimates it. The results for $P4_2/mnm$-TiO_2 are in excellent agreement with previous density functional calculations.[20]

The lattice dynamics of rutile has been the subject of a number of experimental[54−57] and theoretical[20,58] investigations. Traylor et al.[12] used coherent inelastic neutron scattering to measure the phonon dispersion relation along the principal symmetry directions of its Brillouin zone. Furthermore, they determined how the frequency of the transverse optical (TO) A_{2u} mode varies with temperature over the range of 4−300 K. Raman[54,55] and infrared[56] spectroscopies have been used to detect the frequencies of the Γ-point vibrational modes, and the results are in good agreement with the inelastic neutron scattering data. Samara and Peercy[57] have investigated the temperature [(4−500) K] and hydrostatic pressure [(0−4) kbar] dependence of vibrational frequencies of the Raman-active modes B_{1g}, E_g, A_{1g}, and B_{2g}. They also deduced the temperature and pressure dependences of the infrared-active A_{2u} mode from measurements of the static dielectric constants. All of those studies confirm that the A_{2u} mode is always stable.

Our calculated Γ-point phonon frequencies of rutile TiO_2 are collected in Table 4. The results are presented for *Pnnm*-TiO_2 since those for the $P4_2/mnm$ symmetry are not substantially different. In general, for both symmetries, we have obtained (with one exception) positive phonon frequencies. This means that TiO_2 has two minima in the total energy profile but the minimum for *Pnnm*-TiO_2 is lower in energy according to all functionals used in our tests (see Table 3). The PBE functional predicts the frequency of the A_{2u} mode, which is the ferroelectric mode along the *c*-axis, to be imaginary ($\omega = i37.3\ \mathrm{cm}^{-1}$). In other words, according to the PBE functional, TiO_2 rutile is unstable with respect to a distortion along this vibrational mode, and the ground state of rutile is incorrectly predicted to be ferroelectric. The PBEsol functional predicts this frequency to be only slightly positive ($\omega = 68.2\ \mathrm{cm}^{-1}$), in quantitative disagreement with the experimental data. This frequency is, however, well described by the PZ and r++SCAN exchange−correlation functionals. The overall best agreement with the experiment is obtained with the r++SCAN functional especially for higher frequency modes. This gives us additional confidence about the predictive power of the r++SCAN functional with respect to structural properties of rutile TiO_2.

In our previous study focused on the symmetry of β-PbO_2,[28] we have identified the Raman-active mode B_{1g} as the fingerprint of the lowering of symmetry from $P4_2/mnm$ to *Pnnm*. This mode is soft at higher symmetry according to our study. In the case of rutile TiO_2, the frequency of the B_{1g} mode is quite high (see Table 4) and the crystal structure could, in principle, remain stable at the higher symmetry. To further experimentally analyze the symmetry of rutile TiO_2 more precise analyses of Raman spectra should be done in which the different features of the spectrum are not categorized according to the $P4_2/mnm$ symmetry.[59] For instance, the A_{2g} mode which involves a similar lattice distortion as the B_{1g} mode (see Figure 2) is neither Raman-active nor infrared-active according to the $P4_2/mnm$ symmetry; however, it becomes Raman-active if the lower *Pnnm* symmetry is considered.

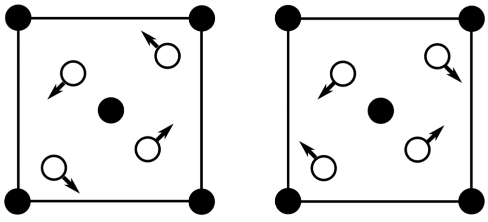
B_{1g} (A_g) A_{2g} (B_{1g})

Figure 2. B_{1g} and A_{2g} modes of vibration (indicated by arrows) of rutile-type TiO_2. The full and empty circles represent Ti and O ions, respectively. In the *Pnnm* symmetry, the modes are classified as A_g and B_{1g}, respectively, and both are Raman-active.

Rietveld Refinements. *Main Structural Results.* We have performed Rietveld refinements of NPD of TiO_2 sample S1 measured at 10, 150 and 300 K as well as Rietveld refinements of SXRPD of samples S1 and S2 at RT. Refinements were done assuming both the tetragonal rutile structure (space group $P4_2/mnm$) and the orthorhombic $CaCl_2$-type structure (space group *Pnnm*). In the unit cell of the $CaCl_2$-type structure, there are two Ti^{4+} ions at (0, 0, 0) and (1/2, 1/2, 1/2) and four O^{2-} ions at (x, y, 0), ($-x$, $-y$, 0), ($1/2 + x$, $1/2 - y$, 1/2), and ($1/2 - x$, $1/2 + y$, 1/2). The structure factors squared for peaks with $h + k + l = 2n$ are equal

$$I_{hkl} \propto \{2f_{\mathrm{Ti}} + 4f_{\mathrm{O}}\cos(2\pi hx)\cos(2\pi ky)\}^2 \tag{3}$$

while for peaks with $h + k + l = 2n + 1$,

$$I_{hkl} \propto \{4f_{\mathrm{O}}\sin(2\pi hx)\sin(2\pi ky)\}^2 \tag{4}$$

The analysis of the orthorhombic $CaCl_2$-type structure is based on the observation of relatively narrow (hhl) peaks with two intensity contributions of equal intensity and at the same position and of slightly broadened (hkl) peaks with $h \neq k$ because of the different positions of (hkl) and (khl) contributions and the different intensity contributions, i.e., $I(hkl) \neq I(khl)$ if $x \neq y$ as given by eqs 3 and 4. In the case of an increasing difference of x and y, one can expect an increasing difference of the intensities $I(hkl)$ and $I(khl)$, i.e., also to an increasing peakshape asymmetry of the merged (hkl) + (khl) peaks observed in the NPD and SXRPD patterns.

For neutrons, $f_{\mathrm{Ti}} = b(\mathrm{Ti}) = -3.438$ fm and $f_{\mathrm{O}} = b(\mathrm{O}) = 5.803$ fm are of different signs, while for X-rays, the atomic form factors of Ti^{4+} and O^{2-} are both positive. This is why for some peaks with $h + k + l = 2n$, the peakshape asymmetry seen with NPD can be reversed compared with that seen with SXRPD (see eq 3). For peaks with $h + k + l = 2n + 1$ (see eq 4), one should observe the same type of peakshape asymmetry both in NPD and SXRPD.

The results of NPD refinements of sample S1 are shown in Tables 5 and 6. The refinements with NPD were done for all Bragg peaks, i.e., for peaks with both even and odd $h + k + l$ sums. The initial setting of $a \geq b$ was chosen in all refinements. Isotropic displacement parameters were refined for both Ti and O.

In every NPD refinement using orthorhombic symmetry of TiO_2, we obtain a positive sign for both r_{ab} and r_{xy} as reported in Table 5. The tetragonal lattice parameters of rutile TiO_2 (both S1 and S2 samples) at RT given in Table 7 agree within less than ±0.001 Å with the results of neutron time-of-flight study of rutile TiO_2 by Burdett et al.[3]

We keep the convention to arbitrarily choose $a \geq b$ for the starting parameters, and in every case, we get $x \geq y$ in the refinement results. The same correlation with positive r_{ab} and r_{xy} signs[1] was observed, e.g., in β-MnO_2, MnF_2,[27] and β-PbO_2[28] at ambient conditions and also in high-pressure studies, e.g., β-MnO_2[60] and NiF_2.[61]

For SXRPD, anisotropic displacement parameters for Ti and isotropic parameters for O were refined. The refinemnent of SXRPD data with all Bragg peaks gives a small difference between x and y oxygen coordinates with relatively large statistical error. This large error is due to the weak dependence of peakshape asymmetry due the difference between $I(hkl)$ and $I(khl)$ on x and y coordinates. This is mainly due to the small

Table 5. Lattice Parameters *a*, *b*, and *c* and Oxygen Coordinates (*x*, *y*, 0) Obtained by Rietveld Refinements of NPD Patterns of Rutile TiO_2 at 300, 150, and 10 K[a][3]

		a (Å)	*b* (Å)	*c* (Å)	*x*	*y*	wRp (%)
ref 3 300 K	tetr.	4.59308(4)	= *a*	2.95889(3)	0.30476(6)	= *x*	
S1−300 K	tetr.	4.59390(10)	= *a*	2.95870(9)	0.3049(2)	= *x*	7.28
S1−300 K	orth.	4.59568(31)	4.59213(31)	2.95870(9)	0.3067(13)	0.3030(14)	7.17
S1−150 K	tetr.	4.58893(10)	= *a*	2.95484(9)	0.3048(2)	= *x*	7.65
S1−150 K	orth.	4.59075(28)	4.58712(28)	2.95484(9)	0.3069(11)	0.3025(12)	7.50
S1−10 K	tetr.	4.58673(10)	= *a*	2.95331(9)	0.3046(3)	= *x*	7.95
S1−10 K	orth.	4.58856(28)	4.58493(27)	2.95331(9)	0.3075(9)	0.3015(10)	7.77
ref 3 15 K	tetr.	4.58666(4)	= *a*	2.95407(3)	0.30469(6)	= *x*	

[a] "tetr." and "orth." refer to the tetragonal $P4_2/mnm$ and the orthorhombic *Pnnm* space groups, respectively. The last column shows the fit quality indicator wRp. The present results are compared with the reference time-of-flight NPD study at 300 and 15 K.[3]

Table 6. Unit Cell Volume, r_{ab} and r_{xy} (See Text) Calculated for Rutile TiO_2 at 300, 150, and 10 K with Parameters from Table 5

		vol (Å^3)	r_{ab}	r_{xy}	wRp (%)
S1−300 K	tetr.	62.4402(25)	0	0	7.28
S1−300 K	orth.	62.4403(35)	0.00077(13)	0.012(8)	7.17
S1−150 K	tetr.	62.2238(25)	0	0	7.65
S1−150 K	orth.	62.2239(34)	0.00079(11)	0.014(7)	7.50
S1−10 K	tetr.	62.1322(25)	0	0	7.95
S1−10 K	orth.	62.1323(34)	0.00079(11)	0.020(6)	7.77

Table 7. Lattice Parameters *a*, *b*, and *c* and Oxygen Coordinates (*x*, *y*, and 0) Obtained by Rietveld Refinements of SXRPD of Rutile TiO_2 Samples S1 and S2 (See Text) at RT[a]

		a (Å)	*b* (Å)	*c* (Å)	*x*	*y*	wRp (%)
ref 3 300 K	tetr.	4.59308(4)	= *a*	2.95889(3)	0.30476(6)	= *x*	
S1-RT	tetr.	4.59379(9)	= *a*	2.95873(6)	0.3052(5)	= *x*	6.83
S1-RT	orth.	4.59565(17)	4.59182(18)	2.95872(6)	0.3059(22)	0.3044(22)	6.30
S1-RT	orth. (odd)	4.59579(17)	4.59239(17)	2.95895(6)	0.3077(13)	0.3037(13)	
S2-RT	tetr.	4.59392(4)	= *a*	2.95881(3)	0.3049(4)	= *x*	9.40
S2-RT	orth.	4.59419(24)	4.59362(25)	2.95881(3)	0.3087(32)	0.3011(32)	9.40
S2-RT	orth. (odd)	4.59435(22)	4.59385(21)	2.95893(3)	0.3065(26)	0.3042(26)	

[a] "tetr." and "orth." refer to the tetragonal $P4_2/mnm$ and the orthorhombic *Pnnm* space groups, respectively. The last column shows the fit quality indicator wRp. Orth(odd) refers to a refinement with $h + k + l$ odd peaks only (see text).

Table 8. Unit Cell Volume, r_{ab} and r_{xy} (See Text), Calculated for Rutile TiO_2 Samples S1 and S2 at RT with Parameters from Table 7

		vol (Å^3)	r_{ab}	r_{xy}	wRp (%)
S1-RT	tetr.	62.4379(20)	0	0	6.83
S1-RT	orth.	62.4360(36)	0.00083(6)	0.005(14)	6.30
S1-RT	orth. (odd)	62.4360(36)	0.00074(5)	0.013(8)	
S2-RT	tetr.	62.4428(8)	0	0	9.40
S2-RT	orth.	62.4426(15)	0.00012(11)	0.026(20)	9.40
S2-RT	orth. (odd)	62.4426(15)	0.00011(9)	0.0070(17)	

value of the *x*- and *y*-dependent part weighted by f_O as compared with the larger contribution weighted by f_{Ti} for $h + k + l$ even (see eq 3). To overcome this problem and try to determine the *x* and *y* coordinates with greater precision, we have performed Rietveld refinements of SXRPD patterns limited to peaks with odd sums $h + k + l = 2n + 1$ only (see eq 4). The results of these refinements are referred to as "orth. (odd)". The results of SXRPD refinements at RT are shown in Tables 7 and 8. The tetragonal lattice parameters of rutile TiO_2 (both S1 and S2 samples) also agree within less than ±0.001 Å with the neutron time-of-flight study by Burdett et al.[3]

The quality fit indicators for the ortorhombic structure are slightly smaller than those for the tetragonal one. Please note that the rutile TiO_2 samples S1 and S2 show considerably different degrees of distortion: r_{ab} = 0.0083(6) and r_{ab} = 0.0012(11), respectively. The observed distortion can be due to sample preparation methods. Similar sample-dependent different degrees of distortion were reported in studies of β-PbO_2,[28] α-Fe_2O_3,[62] and calcite.[63] It is shown in the next sections that despite different numerical values of the distortion, both S1 and S2 samples show an orthorhombically distorted network of Ti−O bonds.

Agreement of Peakshape Asymmetries between NPD and SXRPD Data → Distorted Geometry of Ti−O Bonds. In order to obtain more information about the oxygen ions' positions, we performed Rietveld refinements with for a set of selected fixed x and y coordinates given as

$$x(\xi) = x(\text{avg})\left[1 + \xi\frac{r_{xy}}{2}\right] \tag{5}$$

$$y(\xi) = x(\text{avg})\left[1 - \xi\frac{r_{xy}}{2}\right] \tag{6}$$

where $x(\text{avg})$ is the oxygen position obtained for the tetragonal symmetry and r_{xy} is obtained for the best fit with orthorhombic $CaCl_2$-type structure (see eq 2). The distortion parameter ξ drives the deformation; for $\xi = 0$, we get the tetragonal symmetry with $x = y = x(\text{avg})$, while for $\xi = 1$, we get the best fit orthorhombic structure with $x - y = x(\text{avg})\ r_{xy}$. Rietveld refinements were done by using FullProf.[44] The values of x and y obtained by eqs 5−6 for each ξ were fixed while instrumental peakshape and background parameters were refined. The lattice constants were also refined but kept within $(a - b) \approx a(\text{avg})\ r_{ab} \geq 0$. It means that refinements with $(a - b) < 0$ were discarded. Refinements of the NPD patterns (with all peaks) and SXRPD patterns (with only $h + k + l$ odd peaks) were done for x and y calculated for $-1.6 < \xi < 2.2$ in steps of 0.2. The resulting values of χ^2 versus $x(\text{O})$ for NPD and SXRPD are shown in Figures 3 and 4, respectively. Both NPD and SXRPD data or the S1 sample show a clear minimum of χ^2 near the best orthorhombic solution with $x(\text{O}) \approx 0.3075$ (near $\xi = 1$) located relatively far from the tetragonal value of $x(\text{avg}) = 0.3045$ ($\xi = 0$, shown with a vertical line). The S2 sample SXRPD shows a similar minimum at a slightly different value $x(\text{O}) \approx 0.310$. The agreement of χ^2 minima observed for both NPD and SXRPD is an indication of the orthorhombic distortion of the Ti−O bond geometry of TiO_2 between RT and 10 K. Please keep in mind that the peakshape asymmetry of peaks with $h + k + l$ even is reversed between NPD and SXRPD (see eq 3). Despite this difference due to the negative neutron scattering length of $b(\text{Ti})$, both refinements of NPD and SXRPD data give the same values of $x(\text{O})$ and $y(\text{O})$. It means that the peaks in NPD show a reversed asymmetry as those in SXRPD.

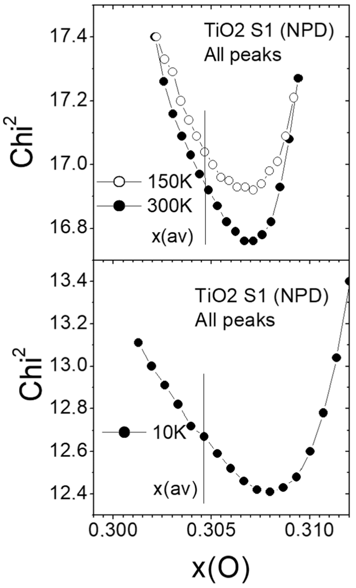

Figure 3. χ^2 vs oxygen coordinate $x(\text{O})$ obtained for rutile TiO_2 sample S1 obtained from NPD at several temperatures using Rietveld refinement for all Bragg peaks (orthorhombic $CaCl_2$-type structure with space group *Pnnm*). The vertical line shows the value of $x(\text{avg})$ (see text).

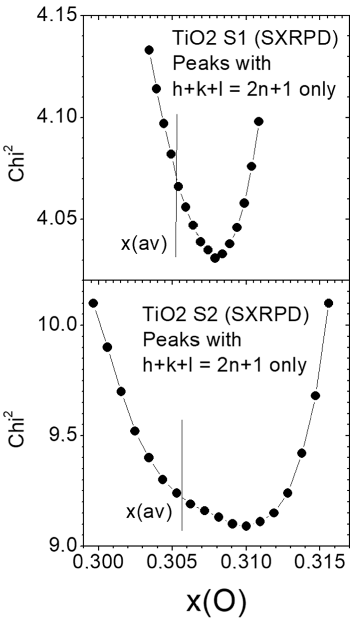

Figure 4. χ^2 vs oxygen coordinate $x(\text{O})$ obtained for rutile TiO_2 samples S1 and S2 obtained from SXRPD at RT using Rietveld refinement for Bragg peaks with $h + k +$ ⟨i⟩l⟨/i⟩ $= 2n + 1$ only (orthorhombic $CaCl_2$-type structure with space group *Pnnm*). The vertical line shows the value of $x(\text{avg})$ (see text).

Agreement of Peakwidths between NPD and SXRPD Data → Similar Orthorhombic Unit Cells. The Bragg peaks from ND and SXRPD patterns, measured with sufficient statistical accuracy, were refined by a pseudo-Voigt profile, given as a function of the scattering angle 2θ. In order to have an approximate description of the instrumental contribution to the peak widths a Caglioti-type,[64] smooth 2θ function given in eq 7 was refined to the observed values $\text{FWHM}_{\text{obs}}(2\theta)$

$$\text{FWHM}_{\text{UVW}}(2\theta) = \{U_{\text{F}} \tan^2(\theta) + V_{\text{F}} \tan(\theta) + W_{\text{F}}\}^{1/2} \tag{7}$$

In a similar way, the observed integral breadth $\beta_{\text{obs}}(2\theta)$ is refined with a similar function

$$\beta_{\text{UVW}}(2\theta) = \{U_\beta \tan^2(\theta) + V_\beta \tan(\theta) + W_\beta\}^{1/2} \tag{8}$$

In principle, one should also add a Lorentzian contribution proportional to $X \tan(\theta)$ for SXRPD data, but it was neglected in order to get a comparable treatment of both SXRPD and NPD data. The refined Cagliotti-type functions, given by eqs 7 and 8 describe the sum of isotropic crystallite-size contributions, isotropic microstrain-type contributions, and the instrumental contributions.

Next, we subtract the refined functions from the observed values in order to get the "corrected" widths

$$\text{FWHM}_{\text{cor}}(2\theta) = \text{FWHM}_{\text{obs}}(2\theta) - \text{FWHM}_{\text{UVW}}(2\theta) \tag{9}$$

$$\beta_{\text{cor}}(2\theta) = \beta_{\text{obs}}(2\theta) - \beta_{\text{UVW}}(2\theta) \tag{10}$$

The FWHM_{cor} and β_{cor} provide information about the anisotropic broadening due to the sample microstructure as discussed, e.g., in refs 65,66. In order to compare peakwidths

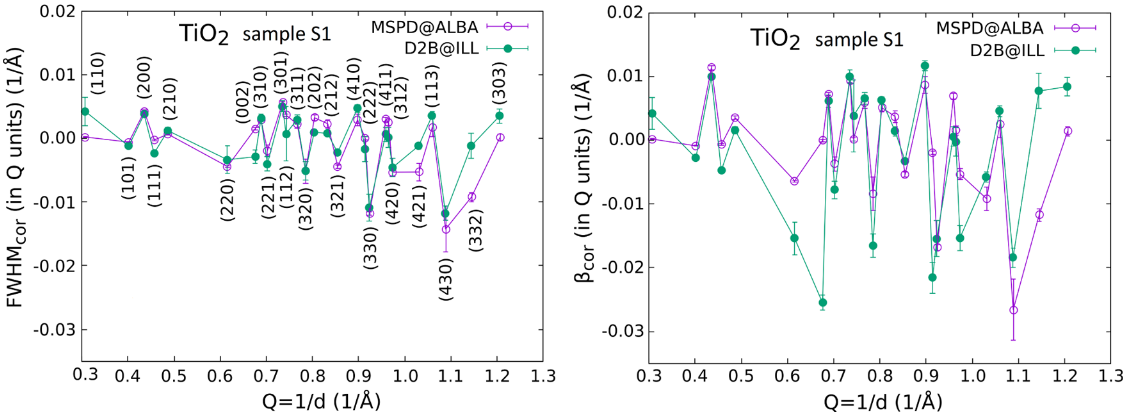

Figure 5. Plot of the peakwidths, i.e., $\mathrm{FWHM_{cor}}(Q)$ (left panel) and $\beta_{cor}(Q)$ (right panel) of Bragg peaks obtained for rutile TiO_2 sample S1 with SXRPD (open symbols) and NPD (solid symbols). Peakwidths are given in Q units ($Å^{-1}$) (see text). The broken lines are shown to guide the eye. Tetragonal (*hkl*) indices are shown in the left panel only.

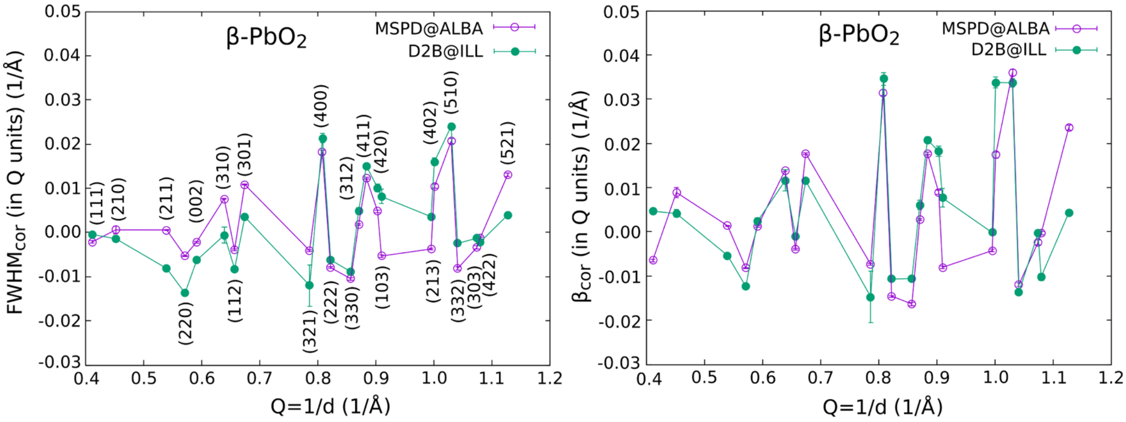

Figure 6. Plot of the peakwidths, i.e., $\mathrm{FWHM_{cor}}(Q)$ (left panel) and $\beta_{cor}(Q)$ (right panel) of Bragg peaks obtained for β-PbO_2 with SXRPD (open symbols) and NPD (solid symbols) data published in ref 28. Peakwidths are given in Q units ($Å^{-1}$) (see text). The broken lines are shown to guide the eye. Tetragonal (*hkl*) indices are shown in the left panel only.

measured at different wavelengths, we transform the widths given in 2θ (in degree units) to the common scale of the scattering vector length, Q, where $Q = (2/\lambda)\sin\theta$ (in $Å^{-1}$)

$$\mathrm{FWHM_{cor}}(Q) = \left(\frac{1}{\lambda}\right)\left(\frac{\pi}{180}\right)\mathrm{FWHM_{cor}}(2\theta)\cos(\theta) \tag{11}$$

$$\beta_{cor}(Q) = \left(\frac{1}{\lambda}\right)\left(\frac{\pi}{180}\right)\beta_{cor}(2\theta)\cos(\theta) \tag{12}$$

The procedure explained above was applied to the present SR and neutron powder diffraction data of rutile (sample S1) TiO_2 at RT (see Figure 5), as well as for older β-PbO_2 data published earlier,[28] also at RT (see Figure 6).

The $\mathrm{FWHM_{cor}}$ and β_{cor} values measured for the same sample at D2B@ILL as well as MSPD@ALBA give satisfactory agreement. The locally most narrow are peaks of (*hhl*)-type, while locally most broad are those of (*h*0*l*)-type. The agreement for $\mathrm{FWHM_{cor}}$ is better than that for β_{cor}.

Taking into account differences in wavelength, about 0.443 and 1.595 Å in SXRPD and NPD, respectively, differences of the illuminated sample size, differences of instrumental resolution, absorption, and other instrumental effects between MSPD@ALBA and D2B@ILL, the quantative agreement of the *hkl*-dependent broadening, i.e., NPD vs SXRDP for both FWHM and β shown in Figures 5 and 6 is a strong indication that the orthorhombic distortion of both oxides is a robust effect.

■ CONCLUSIONS

Neutron and SR diffraction studies as well as DFT calculations demonstrate that rutile TiO_2 has an orthorhombic $CaCl_2$-type structure at temperatures from 10 to 300 K. The DFT calculations based on the plane-wave pseudopotential method and LDA, GGA, and dispersion-corrected exchange−correlation functionals are not sufficiently sensitive to small crystal structure details, whereas more accurate computations based on the highly accurate all-electron FP-LAPW method and LDA, GGA, and meta-GGA (r++SCAN) exchange−correlation functionals confirm the symmetry lowering of rutile TiO_2. The best agreement with the experimental data was obtained by using the r++SCAN functional. We have established that the rutile-type TiO_2 has, in fact, two minima in the total energy profile corresponding to the $P4_2/mnm$ and $Pnnm$ symmetries, but the minimum for $Pnnm$-TiO_2 is lower in energy being, therefore, a global minimum. The lowering of the symmetry brings consequences on the elastic, vibrational, and optical properties of rutile TiO_2. The elastic and optical responses are different along the main crystallographic directions for this material, which was established by calculating the elastic constants and the refractive indices along the *a*-, *b*-, and *c*-axes.

https://doi.org/10.1021/acs.jpcc.3c04573
J. Phys. Chem. C 2023, 127, 19240−19249

For the refractive indices, the relative relationship is $n_b \geq n_a \geq n_c$ although the difference between n_a and n_b is rather modest. The A_{2g} mode, which is neither Raman-active nor infrared-active according to the $P4_2/mnm$ symmetry, becomes Raman-active in the $Pnnm$ symmetry; therefore, this mode may serve as the fingerprint of the rutile TiO_2 symmetry lowering.

■ ASSOCIATED CONTENT

Supporting Information

The Supporting Information is available free of charge at https://pubs.acs.org/doi/10.1021/acs.jpcc.3c04573.

Details about pseudopotential plane-wave-based calculations and calculated vibrational frequencies of the Γ-point phonons (PDF)

Crystallographic information file with RAW experimental data (CIF)

■ AUTHOR INFORMATION

Corresponding Author

Nevill Gonzalez Szwacki − *Faculty of Physics, University of Warsaw, PL-02-093 Warsaw, Poland;* orcid.org/0000-0002-0518-844X; Phone: +48-22-55-32-797; Email: gonz@fuw.edu.pl

Authors

Piotr Fabrykiewicz − *Faculty of Physics, University of Warsaw, PL-02-093 Warsaw, Poland; Institute of Crystallography, RWTH Aachen University, D-52066 Aachen, Germany; Jülich Centre for Neutron Science at Heinz Maier-Leibnitz Zentrum, Forschungszentrum Jülich GmbH, D-85747 Garching, Germany;* orcid.org/0000-0001-7952-2466

Izabela Sosnowska − *Faculty of Physics, University of Warsaw, PL-02-093 Warsaw, Poland;* orcid.org/0000-0002-1574-7225

François Fauth − *CELLS-ALBA, ES-08290 Barcelona, Spain;* orcid.org/0000-0001-9465-3106

Emmanuelle Suard − *Institut Laue-Langevin, F-38042 Grenoble, France;* orcid.org/0000-0001-5966-5929

Radosław Przeniosło − *Faculty of Physics, University of Warsaw, PL-02-093 Warsaw, Poland;* orcid.org/0000-0002-7550-6976

Complete contact information is available at: https://pubs.acs.org/10.1021/acs.jpcc.3c04573

Notes

The authors declare no competing financial interest.

■ ACKNOWLEDGMENTS

The authors acknowledge the Ministry of Science and Higher Education (Poland) for funding. They also acknowledge the Ministry of Science and Higher Education (Poland) for funding access to ILL by Project No. DIR/WK/2018/10. CELLS-ALBA is acknowledged for in-house beam time allocation of Project ID 2020104796. The use of supercomputers at the Interdisciplinary Centre for Mathematical and Computational Modelling (ICM) at the University of Warsaw is also gratefully acknowledged.

■ ADDITIONAL NOTE

^{1}A rotation of the coordinates' system by 90° gives the equivalent structure with $r_{ab} < 0$ and $r_{xy} < 0$.

■ REFERENCES

(1) Baur, W. H. The rutile type and its derivatives. *Crystallogr. Rev.* **2007**, *13*, 65−113.

(2) Cromer, D. T.; Herrington, K. The Structures of Anatase and Rutile. *J. Am. Chem. Soc.* **1955**, *77*, 4708−4709.

(3) Burdett, J. K.; Hughbanks, T.; Miller, G. J.; Richardson, J. W. J.; Smith, J. V. Structural-electronic relationships in inorganic solids: powder neutron diffraction studies of the rutile and anatase polymorphs of titanium dioxide at 15 and 295 K. *J. Am. Chem. Soc.* **1987**, *109*, 3639−3646.

(4) Eddiouane, A.; Chaib, H.; Boussaidi, S.; Nafidi, A.; Zgou, H.; Lmouchter, M.; Tirbiyine, A.; Taoufik, A. Electrical and optical anisotropy in rutile TiO_2. *Ferroelectrics* **2016**, *504*, 204−215.

(5) Radhakrishnan, T. The optical properties of titanium dioxide. *Proc. - Indian Acad. Sci., Sect. A* **1952**, *35*, 117.

(6) Rams, J.; Tejeda, A.; Cabrera, J. M. Refractive indices of rutile as a function of temperature and wavelength. *J. Appl. Phys.* **1997**, *82*, 994−997.

(7) Stephen, L. *Assorted Dimensional Reconfigurable Materials*; Dongre, R. S.; Peshwe, D. R., Eds.; IntechOpen: Rijeka, 2020. Chapter 3.

(8) Fujishima, A.; Honda, K. Electrochemical Photolysis of Water at a Semiconductor Electrode. *Nature* **1972**, *238*, 37−38.

(9) Scanlon, D. O.; Dunnill, C. W.; Buckeridge, J.; Shevlin, S. A.; Logsdail, A. J.; Woodley, S. M.; Catlow, C.; Powell, M. J.; Palgrave, R. G.; Parkin, I. P.; et al. Band alignment of rutile and anatase TiO_2. *Nat. Mater.* **2013**, *12*, 798−801.

(10) Mo, S.-D.; Ching, W. Y. Electronic and optical properties of three phases of titanium dioxide: Rutile, anatase, and brookite. *Phys. Rev. B* **1995**, *51*, 13023−13032.

(11) Kim, S. K.; Choi, G.-J.; Lee, S. Y.; Seo, M.; Lee, S. W.; Han, J. H.; Ahn, H.-S.; Han, S.; Hwang, C. S. Al-Doped TiO_2 Films with Ultralow Leakage Currents for Next Generation DRAM Capacitors. *Adv. Mater.* **2008**, *20*, 1429−1435.

(12) Traylor, J. G.; Smith, H. G.; Nicklow, R. M.; Wilkinson, M. K. Lattice Dynamics of Rutile. *Phys. Rev. B* **1971**, *3*, 3457−3472.

(13) Chen, X.; Selloni, A. Introduction: Titanium Dioxide (TiO_2) Nanomaterials. *Chem. Rev.* **2014**, *114*, 9281−9282.

(14) Zhu, H. Y.; Lan, Y.; Gao, X. P.; Ringer, S. P.; Zheng, Z. F.; Song, D. Y.; Zhao, J. C. Phase Transition between Nanostructures of Titanate and Titanium Dioxides via Simple Wet-Chemical Reactions. *J. Am. Chem. Soc.* **2005**, *127*, 6730−6736.

(15) Yurdakal, S.; Palmisano, G.; Loddo, V.; Augugliaro, V.; Palmisano, L. Nanostructured Rutile TiO_2 for Selective Photocatalytic Oxidation of Aromatic Alcohols to Aldehydes in Water. *J. Am. Chem. Soc.* **2008**, *130*, 1568−1569.

(16) Kubo, T.; Sayama, K.; Nozoye, H. Microfaceting Explains Complicated Structures on Rutile TiO_2 Surfaces. *J. Am. Chem. Soc.* **2006**, *128*, 4074−4078.

(17) Kanehara, K.; Hoshina, T.; Takeda, H.; Tsurumi, T. Terahertz permittivity of rutile TiO_2 single crystal measured by anisotropic far-infrared ellipsometry. *J. Ceram. Soc. Jpn.* **2015**, *123*, 303−306.

(18) Mitev, P. D.; Hermansson, K.; Montanari, B.; Refson, K. Soft modes in strained and unstrained rutile TiO_2. *Phys. Rev. B* **2010**, *81*, No. 134303.

(19) Pascual, J.; Camassel, J.; Mathieu, H. Fine structure in the intrinsic absorption edge of TiO_2. *Phys. Rev. B* **1978**, *18*, 5606−5614.

(20) Montanari, B.; Harrison, N. M. Lattice dynamics of TiO_2 rutile: influence of gradient corrections in density functional calculations. *Chem. Phys. Lett.* **2002**, *364*, 528−534.

(21) Thoa, T. T.; Van Hung, H.; Hue, N. T. M. Study on structural and electronic properties of rutile TiO_2 using DFT+U approach. *Vietnam J. Chem.* **2022**, *60*, 183−189.

(22) Curnan, M. T.; Kitchin, J. R. Investigating the Energetic Ordering of Stable and Metastable TiO_2 Polymorphs Using DFT+*U* and Hybrid Functionals. *J. Phys. Chem. C* **2015**, *119*, 21060−21071.

(23) Zhu, T.; Gao, S.-P. The Stability, Electronic Structure, and Optical Property of TiO_2 Polymorphs. *J. Phys. Chem. C* **2014**, *118*, 11385−11396.

(24) Zhang, Y.; Furness, J. W.; Xiao, B.; Sun, J. Subtlety of TiO_2 phase stability: Reliability of the density functional theory predictions and persistence of the self-interaction error. *J. Chem. Phys.* **2019**, *150*, No. 014105.

(25) Perron, H.; Domain, C.; Roques, J.; Drot, R.; Simoni, E.; Catalette, H. Optimisation of accurate rutile TiO_2 (110), (100), (101) and (001) surface models from periodic DFT calculations. *Theor. Chem. Acc.* **2007**, *117*, 565−574.

(26) Wehinger, B.; Bosak, A.; Jochym, P. T. Soft phonon modes in rutile TiO_2. *Phys. Rev. B* **2016**, *93*, No. 014303.

(27) Fabrykiewicz, P.; Przeniosło, R.; Sosnowska, I.; Fauth, F.; Oleszak, D. Verification of the de Wolff hypothesis concerning the symmetry of β-MnO_2. *Acta Crystallogr., Sect. A: Found. Adv.* **2019**, *75*, 889−901.

(28) Fabrykiewicz, P.; Przeniosło, R.; Gonzalez Szwacki, N.; Sosnowska, I.; Suard, E.; Fauth, F. Orthorhombic symmetry and anisotropic properties of PbO_2. *Phys. Rev. B* **2021**, *103*, No. 064109.

(29) Giannozzi, P.; Baroni, S.; Bonini, N.; et al. QUANTUM ESPRESSO: a modular and open-source software project for quantum simulations of materials. *J. Phys.: Condens. Matter* **2009**, *21*, No. 395502.

(30) The Elk Code, 2023 http://elk.sourceforge.net/. Accessed March 31, 2023.

(31) Perdew, J. P.; Zunger, A. Self-interaction correction to density-functional approximations for many-electron systems. *Phys. Rev. B* **1981**, *23*, 5048−5079.

(32) Perdew, J. P.; Burke, K.; Ernzerhof, M. Generalized Gradient Approximation Made Simple. *Phys. Rev. Lett.* **1996**, *77*, 3865−3868.

(33) Perdew, J. P.; Ruzsinszky, A.; Csonka, G. I.; Vydrov, O. A.; Scuseria, G. E.; Constantin, L. A.; Zhou, X.; Burke, K. Restoring the Density-Gradient Expansion for Exchange in Solids and Surfaces. *Phys. Rev. Lett.* **2008**, *100*, No. 136406.

(34) Furness, J. W.; Kaplan, A. D.; Ning, J.; Perdew, J. P.; Sun, J. Construction of meta-GGA functionals through restoration of exact constraint adherence to regularized SCAN functionals. *J. Chem. Phys.* **2022**, *156*, No. 034109.

(35) Lehtola, S.; Steigemann, C.; Oliveira, M. J. T.; Marques, M. A. L. Recent developments in libxc − A comprehensive library of functionals for density functional theory. *SoftwareX* **2018**, *7*, 1−5.

(36) Fauth, F.; Boer, R.; Gil-Ortiz, F.; Popescu, C.; Vallcorba, O.; Peral, I.; Fullà, D.; Benach, J.; Juanhuix, J. The crystallography stations at the Alba synchrotron. *Eur. Phys. J. Plus* **2015**, *130*, No. 160.

(37) Fauth, F.; Peral, I.; Popescu, C.; Knapp, M. The new Material Science Powder Diffraction beamline at ALBA Synchrotron. *Powder Diffr.* **2013**, *28*, S360−S370.

(38) Bergamaschi, A.; Cervellino, A.; Dinapoli, R.; Gozzo, F.; Henrich, B.; Johnson, I.; Kraft, P.; Mozzanica, A.; Schmitt, B.; Shi, X. The MYTHEN detector for X-ray powder diffraction experiments at the Swiss Light Source. *J. Synchrotron Radiat.* **2010**, *17*, 653−668.

(39) Courbion, G.; Ferey, G. $Na_2Ca_3Al_2F_{14}$: A new example of a structure with "independent F^-"—A new method of comparison between fluorides and oxides of different formula. *J. Solid State Chem.* **1988**, *76*, 426−431.

(40) Roisnel, T.; Rodríquez-Carvajal, J. WinPLOTR: A Windows Tool for Powder Diffraction Pattern Analysis. *Mater. Sci. Forum* **2001**, *378−381*, 118−123.

(41) van Laar, B.; Schenk, H. The development of powder profile refinement at the Reactor Centre Netherlands at Petten. *Acta Crystallogr., Sect. A: Found. Adv.* **2018**, *74*, 88−92.

(42) Rietveld, H. M. A profile refinement method for nuclear and magnetic structures. *J. Appl. Crystallogr.* **1969**, *2*, 65−71.

(43) Petříček, V.; Dušek, M.; Palatinus, L. Crystallographic Computing System JANA2006: General features. *Z. Kristallogr. - Cryst. Mater.* **2014**, *229*, 345−352.

(44) Rodríguez-Carvajal, J. Recent advances in magnetic structure determination by neutron powder diffraction. *Phys. B* **1993**, *192*, 55−69.

(45) Tolba, S. A.; Gameel, K. M.; Ali, B. A.; Almossalami, H. A.; Allam, N. K. *Density Functional Calculations - Recent Progresses of Theory and Application*; InTech, 2018.

(46) Isaak, D. G.; Carnes, J. D.; Anderson, O. L.; Cynn, H.; Hake, E. Elasticity of TiO_2 rutile to 1800 K. *Phys. Chem. Miner.* **1998**, *26*, 31−43.

(47) Manghnani, M. H.; Fisher, E. S.; Brower, W. S. Temperature dependence of the elastic constants of single-crystal rutile between 4° and 583° K. *J. Phys. Chem. Solids* **1972**, *33*, 2149−2159.

(48) Gerward, L.; Olsen, J. S. Post-Rutile High-Pressure Phases in TiO_2. *J. Appl. Crystallogr.* **1997**, *30*, 259−264.

(49) Hill, R. The Elastic Behaviour of a Crystalline Aggregate. *Proc. Phys. Soc., Sect. A* **1952**, *65*, 349−354.

(50) Mouhat, F.; Coudert, F.-X. Necessary and sufficient elastic stability conditions in various crystal systems. *Phys. Rev. B* **2014**, *90*, No. 224104.

(51) Mahmood, T.; Cao, C.; Khan, W. S.; Usman, Z.; Butt, F. K.; Hussain, S. Electronic, elastic, optical properties of rutile TiO2 under pressure: A DFT study. *Phys. B* **2012**, *407*, 958−965.

(52) Mazumder, J. T.; Mayengbam, R.; Tripathy, S. K. Theoretical investigation on structural, electronic, optical and elastic properties of TiO_2, SnO_2, ZrO_2 and HfO_2 using SCAN meta-GGA functional: A DFT study. *Mater. Chem. Phys.* **2020**, *254*, No. 123474.

(53) Amano, T.; Yamazaki, T.; Akashi, R.; Tadano, T.; Tsuneyuki, S. Lattice dielectric properties of rutile TiO_2: First-principles anharmonic self-consistent phonon study. *Phys. Rev. B* **2023**, *107*, No. 094305.

(54) Porto, S. P. S.; Fleury, P. A.; Damen, T. C. Raman Spectra of TiO_2, MgF_2, ZnF_2, FeF_2, and MnF_2. *Phys. Rev.* **1967**, *154*, 522−526.

(55) Balachandran, U.; Eror, N. G. Raman spectra of titanium dioxide. *J. Solid State Chem.* **1982**, *42*, 276−282.

(56) Eagles, D. M. Polar modes of lattice vibration and polaron coupling constants in rutile (TiO_2). *J. Phys. Chem. Solids* **1964**, *25*, 1243−1251.

(57) Samara, G. A.; Peercy, P. S. Pressure and Temperature Dependence of the Static Dielectric Constants and Raman Spectra of TiO_2 (Rutile). *Phys. Rev. B* **1973**, *7*, 1131−1148.

(58) Lee, C.; Ghosez, P.; Gonze, X. Lattice dynamics and dielectric properties of incipient ferroelectric TiO_2 rutile. *Phys. Rev. B* **1994**, *50*, 13379−13387.

(59) Krishnamurti, D. The Raman spectrum of rutile. *Proc. - Indian Acad. Sci., Sect. A* **1962**, *55*, 290−299.

(60) Haines, J.; Léger, J. M.; Hoyau, S. Second-order rutile-type to $CaCl_2$-type phase transition in β-MnO_2 at high pressure. *J. Phys. Chem. Solids* **1995**, *56*, 965−973.

(61) Jorgensen, J. D.; Worlton, T. G.; Jamieson, J. C. Pressure-induced strain transition in NiF_2. *Phys. Rev. B* **1978**, *17*, 2212−2214.

(62) Przeniosło, R.; Sosnowska, I.; Stękiel, M.; Wardecki, D.; Fitch, A.; Jasiński, J. B. Monoclinic deformation of the crystal lattice of hematite α-Fe_2O_3. *Phys. B* **2014**, *449*, 72−76.

(63) Przeniosło, R.; Fabrykiewicz, P.; Sosnowska, I. Monoclinic deformation of calcite crystals at ambient conditions. *Phys. B* **2016**, *496*, 49−56.

(64) Caglioti, G.; Paoletti, A.; Ricci, F. P. Choice of collimators for a crystal spectrometer for neutron diffraction. *Nucl. Instrum.* **1958**, *3*, 223−228.

(65) Popa, N. C. The (hkl) Dependence of Diffraction-Line Broadening Caused by Strain and Size for all Laue Groups in Rietveld Refinement. *J. Appl. Crystallogr.* **1998**, *31*, 176−180.

(66) Stephens, P. W. Phenomenological model of anisotropic peak broadening in powder diffraction. *J. Appl. Crystallogr.* **1999**, *32*, 281−289.